Progress In Electromagnetics Research M, Vol. 116, 119–128, 2023

A Local Two-Port Interferometer to Detect Radio-Vortices at 30 GHz

Lorenzo Scalcinati[1, *], Bruno Paroli[2], Mario Zannoni[1], Massimo Gervasi[1], and Marco A. C. Potenza[2]

Abstract—In this work we show a novel method based on a local two-port interferometer to distinguish the topological charge of radio-vortices at 30 GHz by using a small portion of the entire wavefront only. The experimental investigation of the amplitude and phase properties of the interference pattern with a pure Gaussian beam ($l = 0$) and a $l = 1$ radio vortex is carried out, and results are compared with the theory based on Laguerre-Gauss modes. Experiments were performed both with the interferometer and with single antenna to highlight the effective benefits of the interferometric approach, sensitive to the azimuthal phase of the vortex field. Method is also extendable at higher topological charges for applications to high-density millimetric communications.

1. INTRODUCTION

The affirmation of the singular optics in the last century, also gained with the discovery of radiation carrying Orbital Angular Momentum (OAM) [1–5], brings new challenges in the field of high-density telecommunications with novel methods and technologies applicable to both classical and quantum domains [6].

The orbital angular momentum states of the light are defined as $L_z = l\hbar$, where l is the quantum number (known as topological charge), and $\hbar$ is the Planck constant divided by 2π. In principle, OAM radiation offers an unlimited number of states (being l any integer), a great advantage compared to the polarization states of light.

The large number of accessible states allows to develop effective methods for increasing the information density in communication systems in free space [7] and in fiber [8, 9], by successfully multiplexing and demultiplexing different channels in the variable of the orbital angular momentum, with visible light, infrared light [10], or radio waves [11–14].

In long-distance communications, the natural divergence of radiation imposes fundamental limitations to correctly receive and demultiplex OAM states. In fact, most systems exploit the entire radiation wavefront to properly sort the multiplexed beam in the different channels [15–17], and these methods are not applicable when the receiving antenna is smaller than the beam size. Therefore, the recognition of OAM states in a strictly local way represents a fundamental challenge for long-distance communications.

For example, due to diffraction, at a distance of only 1 km the beam size will be of hundreds of meters (where a beam waist about 1 cm has been assumed for the transmitting antenna). Our research shows that two OAM states (e.g., $l = 1$ and $l = 0$ in our experiment) can be detected by exploiting only a small portion of the radiation beam by using a local interferometer. In this way, information codified in the OAM state can be effectively detected without the need to intercept the entire wavefront. Although the proposed approach has been obtained in a table top experiment, the results open up important perspectives in the field of high density free space communication. In fact, OAM states allow multiplexing and demultiplexing of different channels for high data transfer density.

Received 13 January 2023, Accepted 27 March 2023, Scheduled 17 April 2023

* Corresponding author: Lorenzo Scalcinati (l.scalcinati@campus.unimib.it).

[1] Physics Department, University of Milano Bicocca, Piazza della Scienza 3, Milano 20126, Italy. [2] Dipartimento di Fisica, Universitá degli Studi di Milano, via G. Celoria, 16, Milano 20133, Italy.

Recent works show local detection of OAM states [18–22] or multiplexing and demultiplexing of OAM beams at visible wavelengths, by accessing a small portion of the entire wavefront only and by using a local interferometer as receiver [23]. Other works have been developed in the millimeter wavelength range with the aim of increasing the information that can be transmitted in the same frequency band by using multiplexing and demultiplexing in the variable orbital angular momentum [11–14]. Although these methods are effective, they generally use a substantial portion of the entire wavefront. Conversely, our method is strictly local since, in principle, the locality of detection is only limited by the signal to noise ratio. In particular, these methods exploit the helicity of the radiation wavefront, formally described by the Laguerre Gauss (LG) modes [24]. The LG modes exhibit a dependence of the electric field on the azimuthal angle $E \propto e^{il\theta}$, providing a linear relationship between the phase of the electric field $\phi = l\theta$ and the purely geometrical azimuthal angle θ, where l acts as the constant of proportionality, and i is the complex unit. So in principle, probing the phase of the field at two different angles θ_1, θ_2, we directly obtain the OAM state from the phase difference

$$l = \frac{\phi_2 - \phi_1}{\Delta\theta}, \tag{1}$$

where $\Delta\theta = \theta_2 - \theta_1$ and ϕ_1, ϕ_2 are the phases of the detected field.

In this work, we extend and apply this principle to the millimeter wave range by realizing a local interferometer operating at 30 GHz which allows us to distinguish OAM states by using a small portion of the transmitted beam section ($\approx 20\%$, estimated as the ratio between the effective area of the horn and the area of the beam calculated as πw^2, where w is the transverse beam size on the detection plane). An accurate analysis of the experimental results, obtained with pure Gaussian ($l = 0$) and OAM ($l = 1$) beams, was carried out both in phase and amplitude at different positions from the phase singularity, with particular attention to the contribution of the individual input ports of the interferometer in determining the output field.

The paper is organized as follows. We describe in Section 2 the experimental setup. Results are discussed in Section 3, and finally, we collect our conclusion in Section 4.

2. EXPERIMENTAL SETUP

The experimental setup is shown in Fig. 1. The transmitter and local adding interferometric receiver are mounted on an optical bench shielded with flat radio frequency (RF) absorbers (ECCOSORB HR-10).

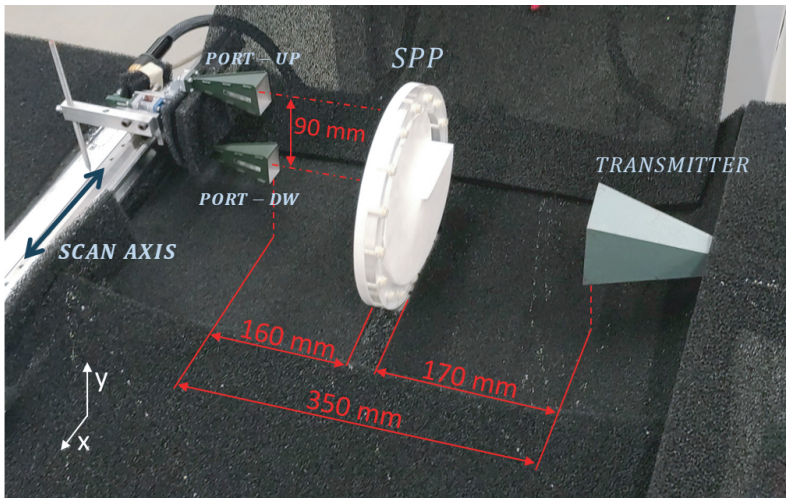

Figure 1. Picture of the experimental setup with the relative distances (between the optical elements) shown in red. The VNA (not shown) is positioned close to the experimental setup and connected with two 1 meter long coaxial cables. Notice that the helicoidal shape of the SPP breaks the cylindrical symmetry of the incident field.

To generate and detect the radiation fields, we use a PNA-X Vector Network Analyser (VNA) N5245A (Agilent Technologies) with port-1 and port-2 connected to the interferometer and to the transmitter, respectively. The transmitter is a WR-28 pyramidal horn antenna with 27 dB gain fed through a waveguide to coax transition and an ultra-flexible GORE RF coaxial cable by the VNA.

A milling machined Spiral Phase Plate (SPP), realized in Polytetrafluoroethylene (PTFE), was used to produce radio-vortices with topological charge $l = 1$ (see Fig. 2). To be machined with a proper shape, two halves have been worked separately, then kept in position by an external polymethylmethacrylate annular frame of 220 mm external diameter. The SPP has a diameter of 170 mm and a maximum depth of 23,9 mm necessary to produce a maximum azimuthal phase shift of 2π when operating at designed frequency (30 GHz). The SPP is positioned along the optical axis of the emitting horn at a distance of 170 mm from the antenna aperture (see Fig. 1 on the right side).

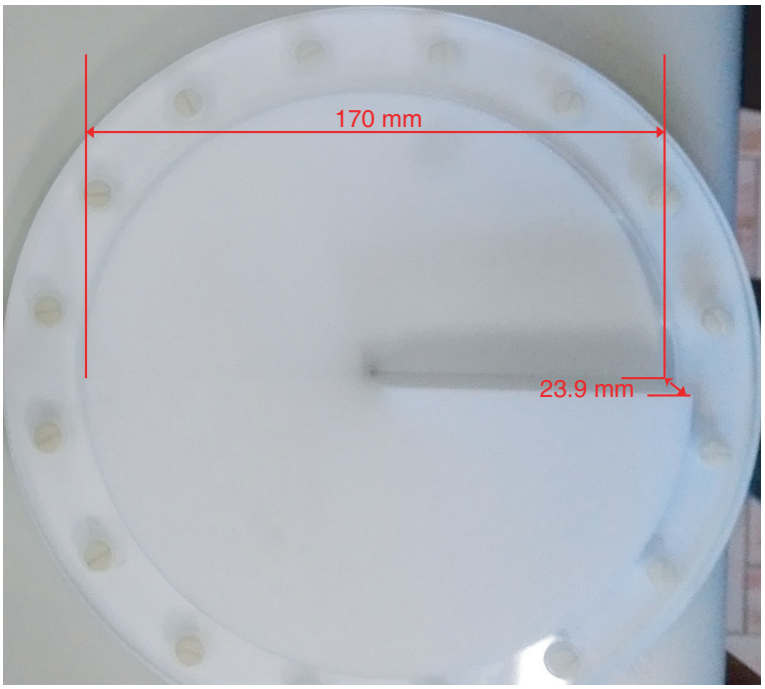

Figure 2. Picture of the Spiral Phase Plate (SPP) used to generate the OAM with $l = 1$. The step length is calculated as $\Delta h = l\lambda/(n-1)$, where λ is the radiation wavelength and n is the refractive index of PTFE.

The interferometer is shown in Fig. 1 (on the left side). It is composed by two WR-28 FLANN standard gain pyramidal horns (20 dB gain), each connected to a WR-28 90-degree bend. The two bends are connected to a symmetric T-junction used as a combiner with equal-phase characteristics. The T-junction output-port is fed through a waveguide to coax transition and a ultra-flexible GORE RF coaxial cable by the VNA. The two horns are separated along the y vertical axis by 90 mm and placed at 160 mm from the SPP. The optical axis is centered on the midpoint of the horns wheelbase. The scattering parameters of the radiation fields were measured at different positions on the x horizontal axis by translating the interferometer along a 110 mm linear path. Scans are performed with a sampling step of 5 mm and 1 mm accuracy. At each scan position the VNA sweeps the frequency of the transmitted field in a narrow band between 29.9 and 30.1 GHz over 101 points with an intermediate frequency (IF) width of 100 Hz.

3. RESULTS AND DISCUSSION

The VNA provides information about the transmitted and received powers through the scattering parameter S_{12} with amplitude $|S_{12}| = 10\text{Log}(\frac{P_1}{P_2})$, where P_2 is the transmitted nominal power from port 2, and P_1 is the power received at port 1. Therefore, the amplitude $|S_{12}|$ provides the normalized power or intensity of the received field in log scale, while the phase ϕ of the received field is computed by the argument of the exponential in $S_{12} = |S_{12}|e^{i\phi}$. In our analysis, both phase and amplitude have been investigated in different configurations to completely characterize the output field at the interferometer when being irradiated by beams with OAM states $l = 0$ and $l = 1$. The experimental data are used to prove that two different OAM states can be distinguished with the proposed local interferometer as predicted by the theory described in [22, 23]. To take into account separately the effects of the fields in the two different horns' positions, corresponding to two different azimuthal values, measurements were also performed by using a single horn, shielding at different times the port UP and the port DW of the interferometer with an ECCOSORB HR-10 absorber. In Fig. 3, we show the intensities for the OAM state $l = 0$ as a function of the scan position. The beam intensity has a Gaussian-like profile when being observed with a single horn at the ports UP and DW (see Fig. 3(a) and Fig. 3(b), respectively).

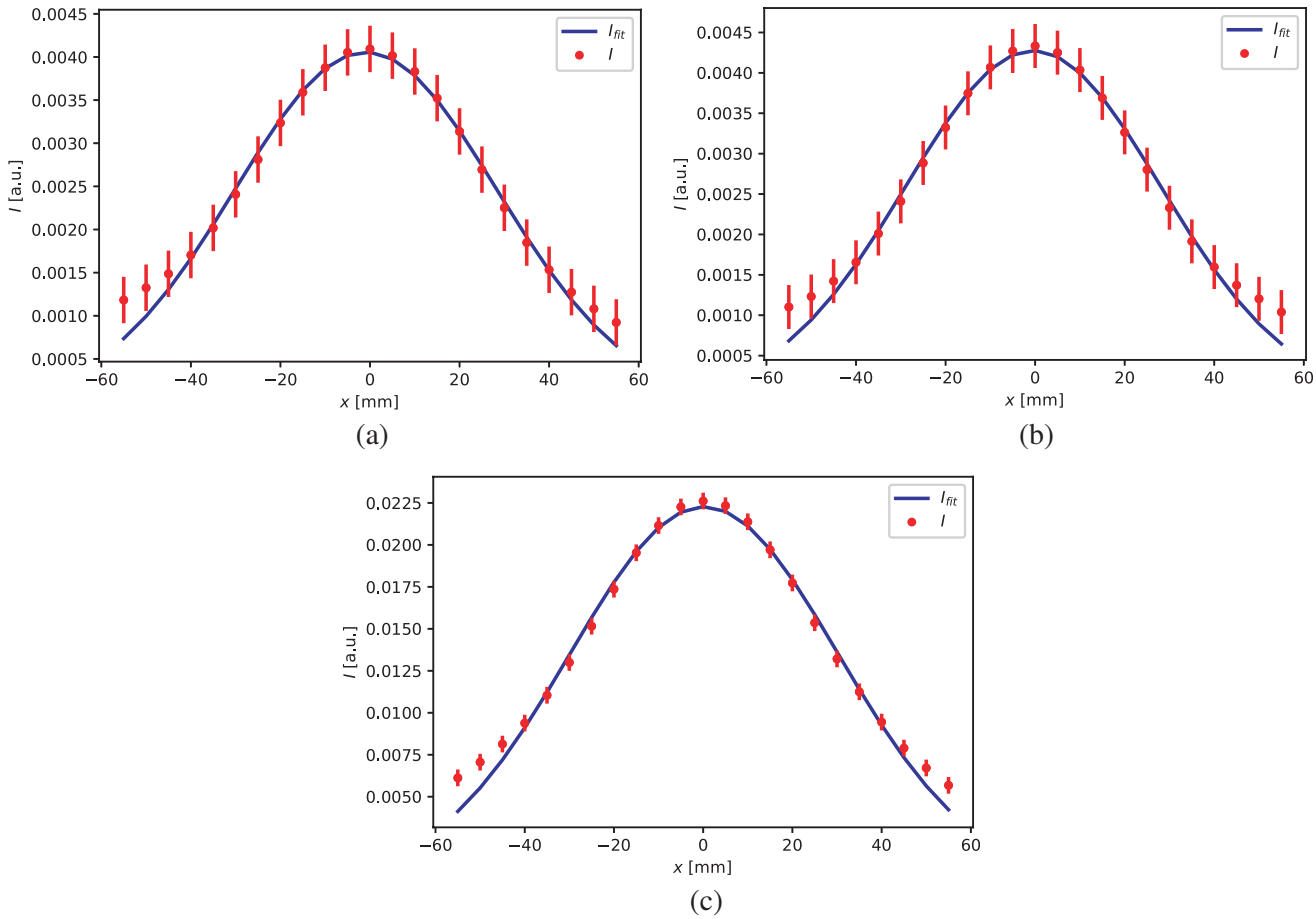

Figure 3. Scans of the intensity profiles of the $l = 0$ LG mode obtained with one single horn (a) up and (b) down and (c) with the interferometer. The blue curves are the model fits of data from −45 to 45 mm as in Eq. (2). The error bars have been estimated from both instrumental and statistical uncertainty.

Data are fitted with the Gaussian beam formula for the intensity

$$I_{fit}(x) = \frac{c}{w^2} \exp\left\{\frac{-2[(x-x_0)^2 + y_0^2]}{w^2}\right\}, \tag{2}$$

where w is the transverse beam size at the beam position $z \approx 350\,\text{mm}$ (i.e., the distance between the interferometer and the transmitter horn apertures), $y_0 = 45\,\text{mm}$ the position of the single port along the vertical axis, c the amplitude fit parameter, and x_0 the x-coordinate of the beam center on the observation plane orthogonal to the propagation axis. In this paper, fits have been performed from -45 to 45 mm in order to exclude deviations from the Laguerre-Gauss model of the tails. The intensity profiles of the single horns (UP and DW) are very similar (except the parameter x_0 that is up to 1 mm, and the other fit parameter differs by up to 5%), confirming the symmetry properties of the waveguide T-junction and the very similar behavior of the two twin horns of the interferometer. Due to the cylindrical symmetry of the Gaussian beam, the interference of the field entering the two ports of the interferometer provides again an output intensity with a Gaussian-like profile as shown in Fig. 3(c). It should be noticed that the maximum intensity received by a single horn is about 20% lower than the expected intensity for the ideal far-field interference process $I_0 = I_{int}/4$, where I_0 is the received single-horn intensity, and I_{int} is the measured intensity due to the interference. Due to the limited propagation distance of the beam, even a small shift can considerably lower the beam efficiency of an antenna. In fact, the efficiency of the off-axis horns decreases to about 80% at the tilt angle of ≈ 4.5 degrees along the vertical axis comparable with the measured angle in our setup.

Moreover, due to this near-field effect, the off-axis antenna does not intercept the maximum power of the Gaussian beam. On the other hand, with the OAM beam, the off-axis receiver antenna intercepts the annular profile close to its maximum intensity, hence the detected intensity of a single-horn will be larger for the OAM beam than that for the Gaussian beam (see Figures 5(a) and (b)).

The phase profiles measured as a function of the scan position are shown in Fig. 4. Here the profiles of the single horns (Figs. 4(a) and (b)) are parabolic as predicted by the Gaussian beam formula for the field

$$\phi_{fit}(x) = -\frac{2\pi}{\lambda}\frac{(x-x_0)^2 + {y_0}^2}{2R} + \phi_0, \tag{3}$$

where R is the radius of curvature of the radiating beam, ϕ_0 an arbitrary additive constant due to the free space propagation of the radiation field, and λ the wavelength of radiation. The fit parameters are x_0, R, ϕ_0.

Notice that the maxima of the phase are not perfectly centered at $x = 0$ due to small geometrical misalignment of the interferometer with respect to the optical axis which implies $x_0 \neq 0$.

Due to the cylindrical symmetry of the Gaussian beam, the interference between the fields entering the two ports (UP and DW) of the interferometer provides an output phase ϕ_{out} equal to that of a single antenna. Since the cylindrical symmetry $\phi_{up} = \phi_{dw}$ and hence

$$A_{out}e^{i\phi_{out}} = A_{up}e^{i\phi_{up}} + A_{dw}e^{i\phi_{dw}} = (A_{up} + A_{dw})e^{i\phi_{up}}, \tag{4}$$

where A_{out} is the amplitude of complex field at the output port of the interferometer; A_{up}, A_{dw} are the amplitudes of the complex fields measured at the output port due to the fields entering the ports UP and DW separately; and ϕ_{up}, ϕ_{dw} are their relative phases.

Equation (4) shows that the interferometer does not introduce substantial topology changes of the amplitude and phase of the fields with respect to a single receiver when the incident beam is characterized by a cylindrical symmetry. A completely different behavior is obtained when an azimuthally dependent field of a radio vortex is received with the local interferometer.

To highlight this behavior we repeat the measurements with the local interferometer by using the $l = 1$ OAM beam generated with the SPP. The intensities as a function of the scan position are shown in Fig. 5. Measurements with single horn (UP and DW) show a profile consistent with the LG modes having radial nodes $p = 0$ and azimuthal mode $l = 1$. The typical annular profile expected for the $l = 1$ LG mode is not observable in our measurements since the scan paths of antennas occur, sampling the top and bottom sides of the ring at its maximum amplitude. Data are fitted with the LG formula:

$$I_{fit}(x) = \frac{c[(x-x_0)^2 + y_0^2]}{w^4} \exp\left\{\frac{-2[(x-x_0)^2 + y_0^2]}{w^2}\right\}, \tag{5}$$

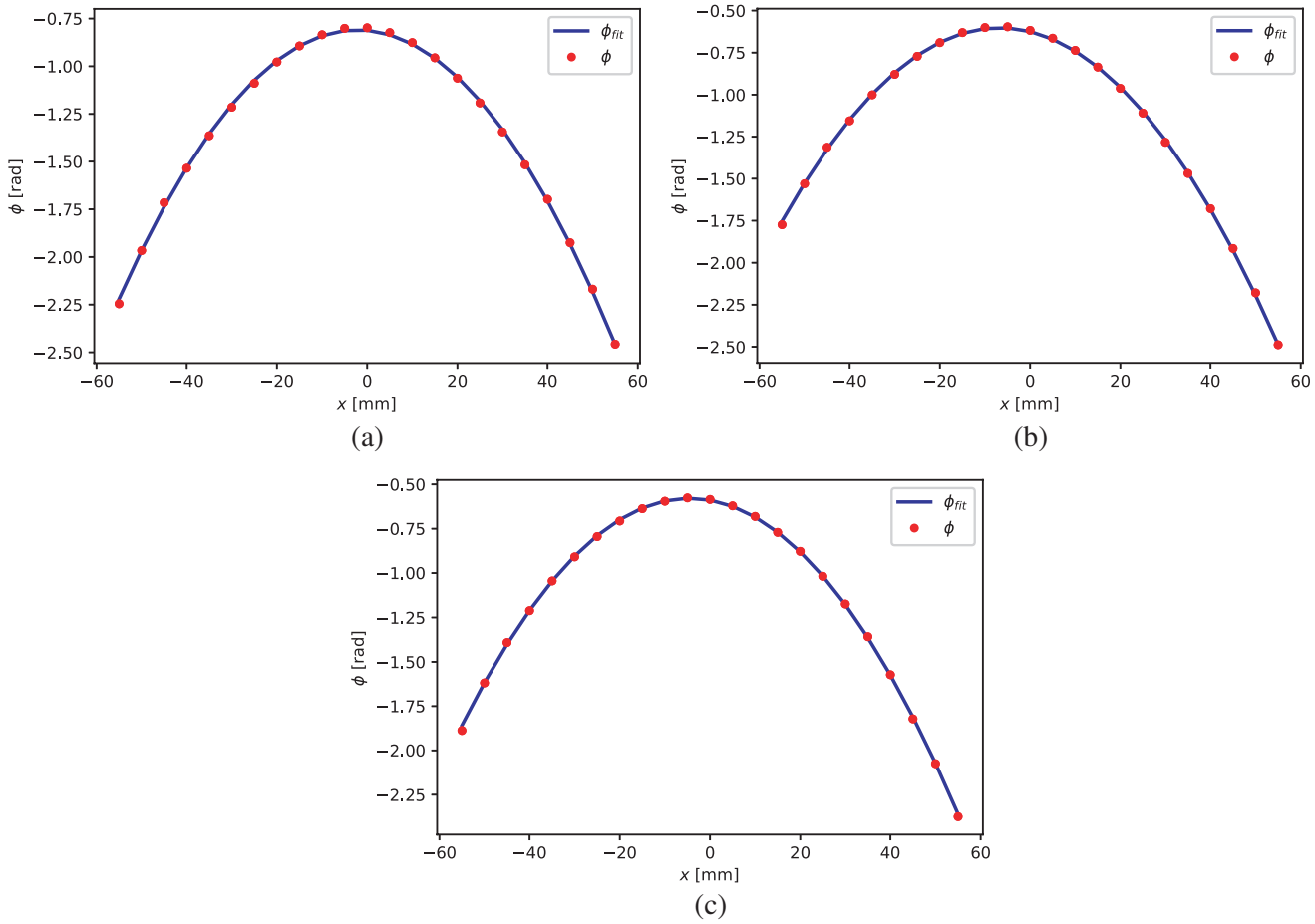

Figure 4. Scans of the phase profiles of the $l = 0$ LG mode obtained with the single horn (a) up and (b) down and (c) with the interferometer. The blue curves are the model fits of data from -45 to 45 mm as in Eq. (3). Notice that the phase profiles (a) and (b) are displaced (with respect to the propagation axis) of about -2 mm and -7 mm, respectively. This effect is probably related to small misalignments of the horn phase center. The error bars values (not shown) are $\sigma_a = 0.015$ rad, $\sigma_b = 0.012$ rad and $\sigma_c = 0.010$ rad for (a), (b) and (c), respectively.

where the quadratic factor $[(x - x_0)^2 + y_0^2]$, on the left of the exponential, is responsible for the annular radial profile. Notice that for $y_0 \approx 45$ mm the intensity profile has a single maximum as observed experimentally.

A completely different intensity profile is observed by using the interference of the fields entering the two horns. In fact, as predicted by Eq. (1), the OAM states provide a phase difference $\Delta\phi$ affecting the LG intensity profile of Eq. (5) as follows

$$I_{int}(x) = \frac{2c[(x - x_0)^2 + y_0^2]}{w^4} \exp\left\{\frac{-2[(x - x_0)^2 + y_0^2]}{w^2}\right\}(1 + \cos\Delta\phi)\,, \tag{6}$$

where $(1 + \cos\Delta\phi)$ is the extra-factor due to the interference of the fields entering the two horns UP and DW centered on θ_1 and θ_2, respectively and

$$\Delta\phi = -2\arccos\left\{\frac{x - x_0}{\sqrt{(x - x_0)^2 + y_0^2)}}\right\}. \tag{7}$$

The experimental results are shown in Fig. 5(c). Notice that the states $l = 0$ and $l = 1$ are distinguishable from the intensity of the interferometer, also assuming different normalization factors,

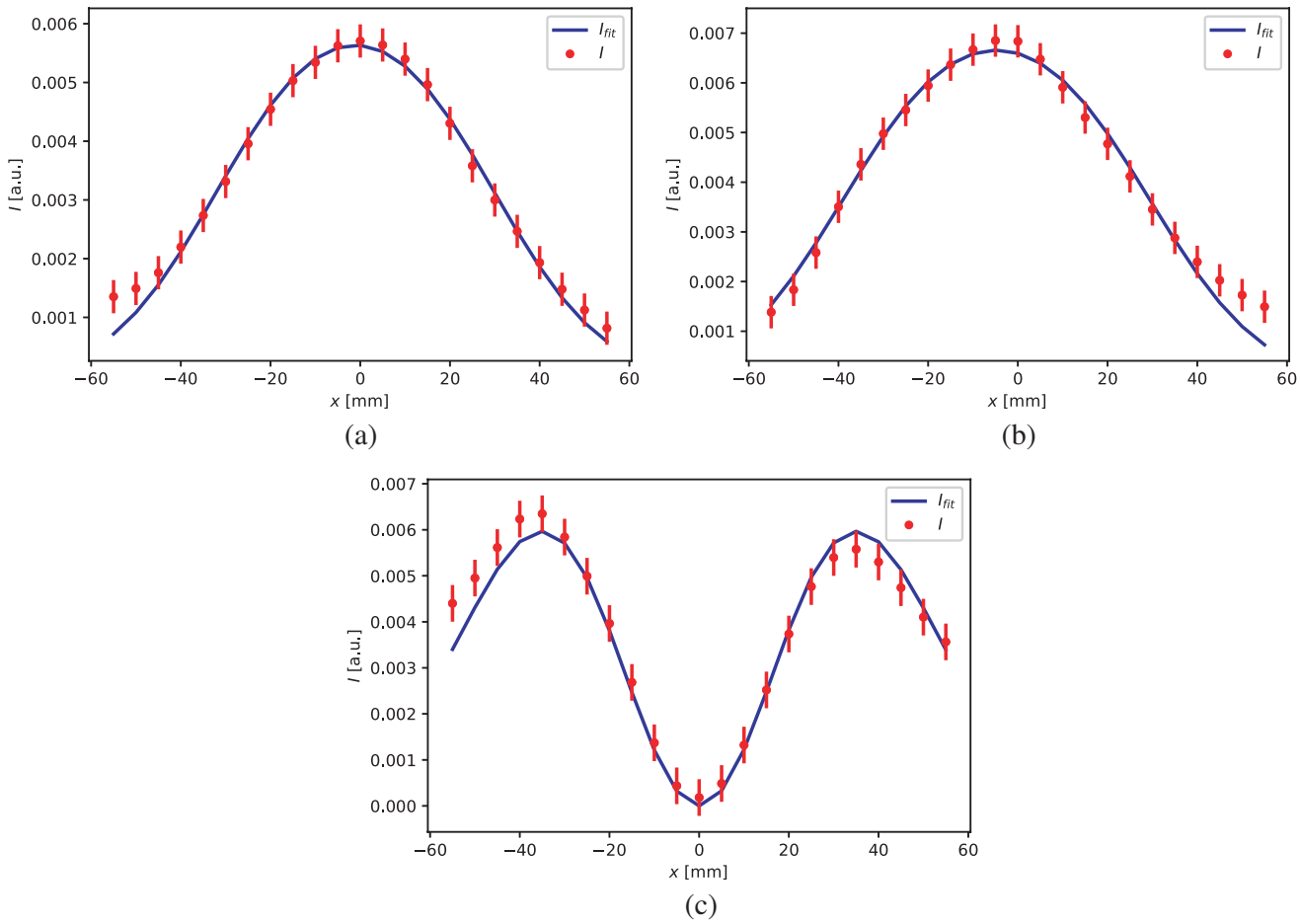

Figure 5. Scans of the intensity profiles of the $l = 1$ LG mode obtained with the single horn (a) up and (b) down and (c) with the interferometer. The blue curves are the model fits of data from -45 to 45 mm as in Eq. (5) for (a) and (b) and in Eq. (6) for (c). The error bars have been estimated from both instrumental and statistical uncertainty.

being the shape of the intensity profiles of the $l = 0$ mode in Fig. 3(c) completely different with respect to the intensity profile of the $l = 1$ mode in Fig. 5(c). Furthermore, we stress that to distinguish different OAM states, scans are not strictly necessary as shown in the analogous case with visible light [23], and in fact, the intensity changes (at the output port of the interferometer) depending on l, even for a fixed position x, being the interferometer sensible to the phase difference $l\Delta\theta$ and not to the amplitudes of the LG modes only. As an example this occurs in our experimental data, at $x = 0$.

In order to have a deeper understanding of the interference processes with OAM beams, we report in Fig. 6 the measurements of the phase of the fields received with single horn and with the interferometer as a function of the scan position, for the OAM state $l = 1$. Here the phase profiles are obtained compensating the effect of the wavefront curvature with the difference $\phi = \phi_M - \phi_G$, where ϕ is the compensated phase profile, ϕ_M the measured phase profile, and ϕ_G the phase profile measured with the $l = 0$ mode (see Fig. 4). The compensated phase profiles of the single antennas are in good agreement with the expected functions obtained considering the phase of the field of the $l = 1$ mode, along the scan paths of the two horns (up and down), given by

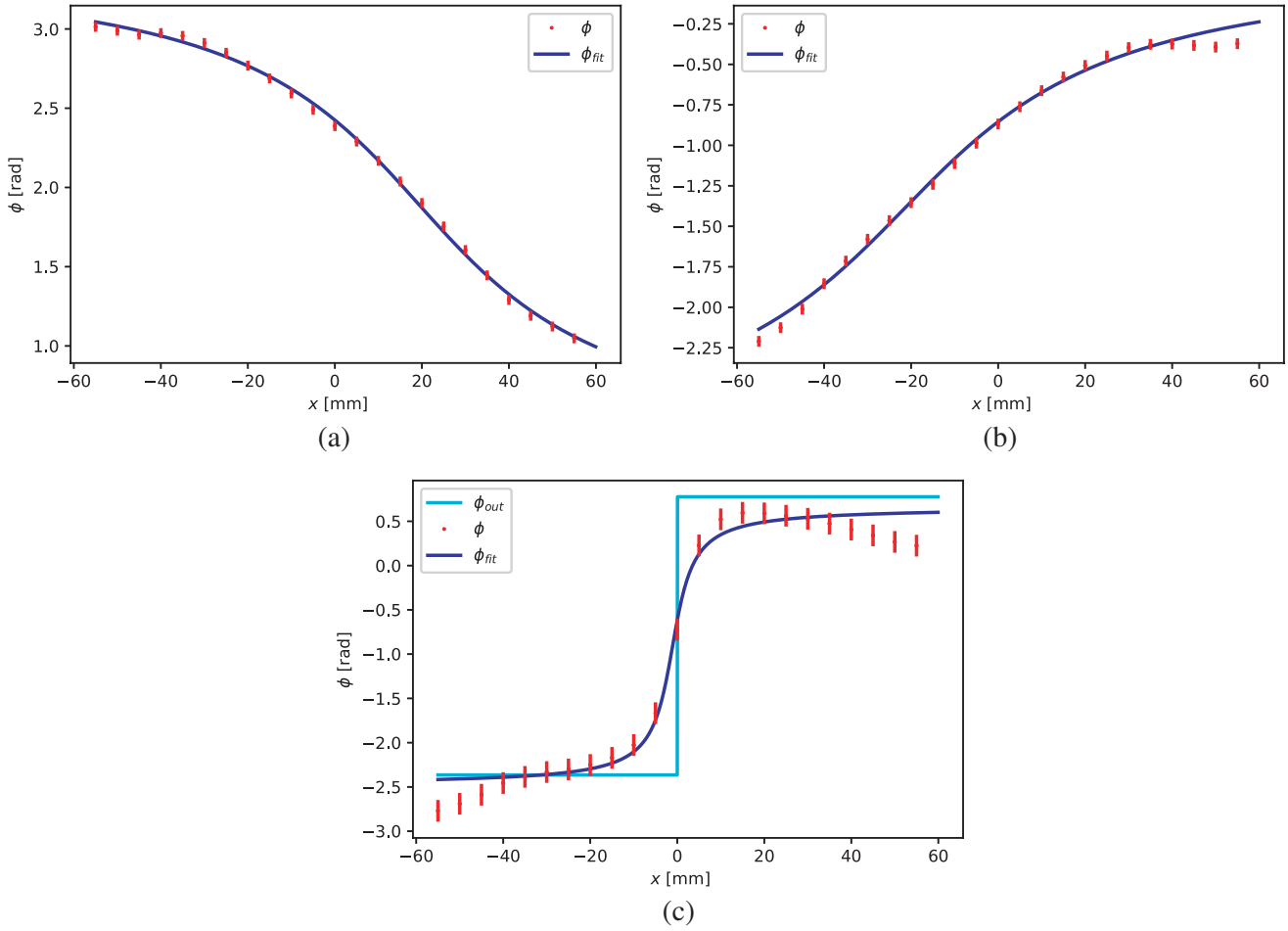

Figure 6. Scans of the phase profiles of the $l = 1$ LG mode obtained with the single horn (a) up and (b) down and (c) with the interferometer. The blue curves are the model fits of data from −45 to 45 mm as in Eq. (8) for (a), (b) and (c), while the cyan curve is the fit model as in Eq. (10). Notice that the phase profiles (a) and (b) are displaced (with respect to the propagation axis) of about 19 mm and −21 mm, respectively. This effect is probably related to asymmetrical refraction from the SPP and to small misalignments of the horn phase center. The error bars have been estimated from both instrumental and statistical uncertainty.

$$\phi_{fit}(x) = \begin{cases} -\arccos\left\{\dfrac{x - x_0}{\sqrt{(x-x_0)^2 + y_0^2)}}\right\} + \phi_0 & DW \\ \arccos\left\{\dfrac{x - x_0}{\sqrt{(x-x_0)^2 + y_0^2)}}\right\} + \phi_0 & UP \end{cases}, \tag{8}$$

with fit parameters x_0, y_0, and ϕ_0.

The theoretical phase profile of the compensated interference field is deduced similarly to Eq. (4), but by taking into account the azimuthal phase of the $l = 1$ mode as

$$A_{out} e^{i\phi_{out}} = A_{up} e^{il\theta_1} + A_{dw} e^{il\theta_2}, \tag{9}$$

with the assumptions $l = 1$, $\theta_2 = 2\pi - \theta_1$, and $A_{up} = A_{dw}$, we find

$$\phi_{out} = \begin{cases} \phi_0 & x < 0 \\ \pi + \phi_0 & x > 0 \end{cases}, \tag{10}$$

where ϕ_0 is an additive phase due to the free propagation of the radiation field from the transmitter to the receiving antennas. This result is in qualitative agreement with the experimental data shown in Fig. 6(c). Here the phase profile is close to a step function centered on $x = 0\,\text{mm}$, with a phase difference of $\approx \pi$ rad between the phases at $x > 0$ and $x < 0$, and a rapid phase change close to $x = 0$.

4. CONCLUSIONS

In this work, we have shown that two OAM states can be distinguished at 30 GHz by accessing a small portion of the entire wavefront only ($\approx 20\%$). An experimental setup has been realized in order to characterize, through the scattering parameters, the amplitude and phase properties of the fields of an $l = 0$ and $l = 1$ radio vortices detected both with single antenna and with a local adding interferometer. Results are in good agreement with the expectation model functions obtained with the corresponding Laguerre-Gauss modes. In particular, with $l = 1$, two intensity lobes are observed at the interferometer output as a consequence of the azimuthal phase properties and not as a consequence of the annular intensity profile. This confirms that the interferometer is sensible to the topological charge by means of the phase difference $\phi_2 - \phi_1$ as shown in Eq. (1).

While we performed a complete scan of the interference pattern for a better comparison with the theory, results show that the two states are well distinguishable also at a fixed position of the local interferometer.

In agreement with Eq. (1), due to the cylindrical symmetry of the Gaussian beam, the phase difference $\phi_2 - \phi_1$ tends to be zero for $l = 0$; therefore, constructive interference is observed at $x = 0$, and a maximum of intensity is measured. With the radio vortex, the phase difference is $\phi_2 - \phi_1 \approx \pi$, which induces a minimum of intensity at $x = 0$ and causes a substantial decrease $\approx -21\,\text{dB}$ of the interferometer intensity with respect to the $l = 0$ state (at the same observation position). This allows to distinguish the two OAM states $l = 0$ and $l = 1$ with high signal-to-noise-ratio (≈ 16), where the signal is the difference between the intensities of the $l = 0$ and $l = 1$ states, while the noise is $\sqrt{\sigma_{stat}^2 + \sigma_{inst}^2}$, where σ_{stat} is the statistical uncertainty, and σ_{inst} is the instrumental uncertainty for the intensity of the $l = 0$ mode (worst case).

The proposed method can be extended to higher topological charges, in order to increase the number of states (and hence the information) that can be transferred in the same frequency band, with potential applications to high density communication systems. Of course, the number of possible states is limited by the number of the corresponding intensity levels that can be effectively separated at the interferometer output, without overlapping between neighboring levels due to noise.

REFERENCES

1. Coullet, P., L. Gil, and F. Rocca, "Optical vortices," *Opt. Commun.*, Vol. 73, 403–408, 1989.
2. Brambilla, M., L. A. Lugiato, V. Penna, F. Prati, C. Tamm, and C. O. Weiss, "Transverse laser patterns. II. Variational principle for pattern selection, spatial multistability, and laser hydrodynamics," *Phys. Rev. A*, Vol. 43, 5114, 1991.
3. Bazhenov, V. Yu., M. V. Vasnetsov, and M. S. Soskin, "Laser beams with screw dislocations in the wavefronts," *Pis'ma Zh. Eksp. Teor. Fiz.*, Vol. 52, 1037–1039, 1990.
4. Bazhenov, V. Yu., M. S. Soskin, and M. V. Vasnetsov, "Screw dislocations in light wavefronts," *J. Mod. Optics*, Vol. 39, 985–990, 1992.
5. Allen, L., M. W. Beijersbergen, R. J. C. Spreeuw, and J. P. Woerdman, "Orbital angular momentum of light and the transformation of Laguerre-Gaussian laser modes," *Phys. Rev. A*, Vol. 45, 8185, 1992.
6. Willner, A. E., K. Panga, H. Song, K. Zou, and H. Zhou, "Orbital angular momentum of light for communications," *Appl. Phys. Rev.*, Vol. 8, 041312, 2021.

7. Willner, A. E., Y. Ren, G. Xie, Y. Yan, L. Li, Z. Zhao, J. Wang, M. Tur, A. F. Molisch, and S. Ashrafi, "Recent advances in high-capacity free-space optical and radio-frequency communications using orbital angular momentum multiplexing," *Philos. Trans. A Math. Phy. Eng. Sci.*, Vol. 375, 20150439, 2017.
8. Cozzolino, D., D. Bacco, B. Da Lio, K. Ingerslev, Y. Ding, K. Dalgaard, P. Kristensen, M. Galili, K. Rottwitt, S. Ramachandran, and L. K. Oxenløwe, "Orbital angular momentum states enabling fiber-based high-dimensional quantum communication," *Phys. Rev. App.*, Vol. 11, 064058, 2019.
9. Wang, J., S. Chen, and J. Liu, "Orbital angular momentum communications based on standard multi-mode fiber," *APL Photonics*, Vol. 6, 060804, 2021.
10. Ren, Y., L. Li, Z. Wang, et al., "Orbital angular momentum-based space division multiplexing for high-capacity underwater optical communications," *Sci. Rep.*, Vol. 6, 33306, 2016.
11. Yan, Y., G. Xie, M. Lavery, et al., "High-capacity millimetre-wave communications with orbital angular momentum multiplexing," *Nat. Commun.*, Vol. 5, 4876, 2014.
12. Hui, X., S. Zheng, Y. Chen, et al., "Multiplexed millimeter wave communication with dual Orbital Angular Momentum (OAM) mode antennas," *Sci. Rep.*, Vol. 5, 10148, 2015.
13. Allen, B., D. Simmons, T. D. Drysdale, and J. Coon, "Performance analysis of an orbital angular momentum multiplexed amplify-and-forward radio relay chain with inter-modal crosstalk," *R. Soc. Open Sci.*, Vol. 6, 181063, 2019.
14. Assimonis, S. D., M. A. B. Abbasi, and V. Fusco, "Millimeter-wave multi-mode circular antenna array for uni-cast multi-cast and OAM communication," *Sci. Rep.*, Vol. 11, 4928, 2021.
15. Mirhosseini, M., M. Malik, Z. Shi, and R. W. Boyd, "Efficient separation of the orbital angular momentum eigenstates of light," *Nat. Commun.*, Vol. 4, 2781, 2013.
16. Li, C. and S. Zhao, "Efficient separating orbital angular momentum mode with radial varying phase," *Opt. Express*, Vol. 5, 267–270, 2017.
17. Berkhout, G. C. G., M. P. J. Lavery, J. Courtial, M. W. Beijersbergen, and M. J. Padgett, "Efficient sorting of orbital angular momentum states of light," *Phys. Rev. Lett.*, Vol. 105, 153601, 2010.
18. Paroli, B., A. Cirella, I. Drebot, V. Petrillo, M. Siano, and M. A. C. Potenza, "Asymmetric lateral coherence of OAM radiation reveals topological charge and local curvature," *Journal of Optics*, Vol. 20, 1–10, 2018.
19. Paroli, B., M. Siano, and M. A. C. Potenza, "The local intrinsic curvature of wavefronts allows to detect optical vortices," *Opt. Express*, Vol. 27, 17550, 2019.
20. Scalcinati, L., B. Paroli, M. Zannoni, and M. A. C. Potenza, "Measurement of the local intrinsic curvature of a $l = 1$ radio-vortex at 30 GHz," *Progress In Electromagnetic Research M*, Vol. 94, 1–8, 2020.
21. Paroli, B., M. Siano, and M. A. C. Potenza, "Measuring the topological charge of orbital angular momentum radiation in single-shot by means of wavefront intrinsic curvature," *Appl. Opt.*, Vol. 59, 5258, 2020.
22. Paroli, B., M. Siano, and M. A. C. Potenza, "A composite beam of radiation with orbital angular momentum allows effective local, single-shot measurement of topological charge," *Opt. Commun.*, Vol. 459, 2020.
23. Paroli, B., M. Siano, and M. A. C. Potenza, "Dense-code free space transmission by local demultiplexing optical states of a composed vortex," *Opt. Express*, Vol. 29, 14412–14424, 2021.
24. Koksal, K., M. Babiker, V. E. Lembessis, and J. Yuan, "Chirality and helicity of linearly-polarised Laguerre-Gaussian beams of small beam waists," *Opt. Commun.*, Vol. 490, 126907, 2021.